

Article

Cavity Behavior of Fine-Grained 5A70 Aluminum Alloy during Superplastic Formation

Sheng Li , Shunyao Jin  and Zhongguo Huang * 

School of Mechanical Engineering, University of Science and Technology Beijing, Beijing 100083, China; lishengsir@163.com (S.L.); jinshunyao@ustb.edu.cn (S.J.)

* Correspondence: jsy_white@126.com; Tel.: +86-010-6233-2467

Received: 18 November 2018; Accepted: 12 December 2018; Published: 14 December 2018



Abstract: The study of the exact physical mechanism of cavity nucleation and growth is significant in terms of predicting the extent of internal damage following superplastic deformation. The 5A70 alloy was processed by cold rolling for 14 passes with a total reduction deformation of 90% (20–2 mm) and the heat treatment was inserted at a thickness of 10 and 5 mm at 340 °C for 30 min. The superplastic tensile tests were performed at 400, 450, 500, 550 °C and the initial strain rate was $1 \times 10^{-3} \text{ s}^{-1}$. Cavities were observed at the head of the particle and the interface of the grain boundaries. It is suggested that the cavity was nucleated during the sliding/climbing of the dislocations, due to the precipitate pinning effect and the impeding grain boundary during grain boundary sliding (GBS). In this study, the results demonstrated a clear transition from diffusion growth to superplastic diffusion growth and plastic-controlled growth at a cavity radius larger than 1.52 and 13.90 μm . The cavity nucleation, growth, interlinkage and coalescence under the applied stress during the superplastic deformation, as well as the crack formation and expansion during the deformation, ultimately led to the superplastic fracture.

Keywords: 5A70 aluminum alloy; superplastic tensile; cavity growth; fracture

1. Introduction

The massive magnesium solid solution from the dispersion phase and the magnesium content in aluminum alloys improve the strength properties, fatigue strength, wear resistance, joint properties and the forming properties [1–3]. Aluminum alloys have been extensively researched with regard to superplastic formation due to their non-heat-treatment properties. In recent decades, aluminum alloy superplastic structures have been cited in the locations of Su-27, MIG-26 and J-10 stamping parts such as the fuselage, stringer, vertical tail skin, etc. [4]. It is well known that aluminum alloys exhibit superplastic fractures due to the presence of the cavity caused by the Mg-rich phase particles. However, most early studies related a less than 5 mass% magnesium content of aluminum alloys with excellent elongation.

Numerous researchers have reported the superplasticity of the Al–Mg series aluminum alloys [5–8], super-strength aluminum alloys (Al–Mg–Cu series) [9,10] and ultra-high-strength aluminum alloys (Al–Zn–Mg–Cu series) using equal channel angular pressing (ECAP), friction stir processing (FSP) and high-pressure rotation (HPT) methods [11–14]. It demonstrates that superplastic flow can be achieved in aluminum alloy with small grain sizes, typically less than 10 μm . In order to satisfy the requirement of a 2 mm thickness of superplastic stamping products, the precipitated phases in the ingot casting billet were controlled, combined with heat treatment between the cold rolling of the 5A70 aluminum alloy. The obtained superplastic elongation-to-failure value, δ , was greatly improved when compared to the existing commercial sheets [15].

In this study, attention was focused on the exact mechanism of cavity nucleation and cavity growth during the superplastic deformation to study the cavity behavior in detail. The cavity behavior found at different tensile stages and in different superplastic fractures were precisely identified via supporting microscopy evidence. However, cavitation is a function of external factors such as temperatures and grain sizes, which are both related to the second phase particles. It was found that the cavity nucleation, growth, interlinkage and coalescence during superplastic deformation were caused extensively by the precipitated phase [16–20].

2. Materials and Methods

The chemical composition of the 5A70 alloy is shown in Table 1. The prepared experimental alloy ingot was homogenized and annealed at 450 °C for 40 h. Then the ingot alloy was rolled into a billet with a rectangular normal direction plane of 255 mm × 255 mm at 380 °C. From the state of the extruding ingot, a billet with a plate shape (200 mm × 200 mm × 25 mm) was processed, and the natural aging treatment was ≥ 240 h. The size and distribution of the precipitated phases in the smelted and forged processes were controlled to promote the nucleation during dynamic recrystallization, and the billet was subjected to 14 passes of cold rolling on a 350 mm reversing cold mill, and full recrystallization was inserted when the sheet was 10 and 5 mm thick using a GS-2-1200 box-type resistance furnace (Tianjin Zhonghuan Lab Furnace Co., Ltd., Tianjing, China). Ultimately, the 2 mm thickness of fine-grained (FG) 5A70 alloy superplastic sheet was obtained, and the initial grain size of the rolling direction plane was 8.48 μm . Further details of the rolling process and the full recrystallization system were reported in a previous work [15].

Table 1. Chemical compositions of the studied 5A70 aluminum alloy (wt.%).

Mg	Fe	Cu	Si	Zn	Ti	Mn	Al
5.72	0.20	0.058	0.080	0.020	0.043	0.60	Bal.

Specimens with 8 mm gage length and 4 mm gage width were machined in the parallel rolling direction. Superplastic tensile tests were performed on an AG-250KINC Instron machine (Shanghai Gold Casting Instrument Analysis Co., Ltd., Shanghai, China) with a microprocessor control pad in the NV63-CV high temperature furnace. The tests were performed at different temperatures ranged from 400 to 550 °C, and the initial strain rate was $1 \times 10^{-3} \text{ s}^{-1}$ in an air condition. In addition, type-K thermocouples were used to detect the furnace and the temperature was controlled within approximately ± 2 °C along the entire gage length during the tests. The specimen was insulated at 340 °C and 10 min for full recrystallization; moreover, it can control the temperature equilibrium during the heating process. Immediately, the same heating rate, 21 °C/min, was utilized to reach the target temperature and maintained for 2 min.

The microstructural characterization and analysis of the 5A70 alloy were carried out using a Jeol-7100 (JEOL Ltd., Tokyo, Japan) transmission electron microscope (TEM) and a 600FEG (FEI Corporation, Hillsboro, OR, USA) scanning electron microscope (SEM) or structural characterization analysis. The average grain size was found using the linear intercept method and the OIM software (6.2.0 x86 version, EDAX Inc., Draper, UT, USA). The boundary orientation was measured by utilizing pixel-to-pixel measurements. To carry out the structural characterization, specimens of the SEM were cut 5 mm from the superplastic fracture surface.

3. Results and Discussion

3.1. Superplastic Tensile Tests

It is known that 5A70 aluminum alloy is non-heat treatable with the dissolution and melting temperature is 556 and 631 °C, respectively. Superplastic tensile tests focused on investigating the states of cavity in superplastic deformation of the studied 5A70 alloy. Superplastic tensile tests of

FG 5A70 alloy were performed at an initial strain rate of $1 \times 10^{-3} \text{ s}^{-1}$ and the temperatures ranged from 400 to 550 °C, according to relevant literature and thermal analysis experimental results [21]. The true stress–true strain results of the superplastic tensile tests are shown in Figure 1a. At a constant strain rate, the strain enhancement phenomenon of the materials was consistent with the general law of superplastic elongation characteristics and increased temperature. Meanwhile, three more tensile tests were carried out and the tensile deformations were unloading at the strain $\varepsilon = 0.65, 1.40$ and 2.65, when the superplastic tensile test temperature was 500 °C and the strain rate was $1 \times 10^{-3} \text{ s}^{-1}$. The intermediate state of the deformation structures was obtained using water quenching, and the engineering stress–engineering strain results are shown in Figure 1b.

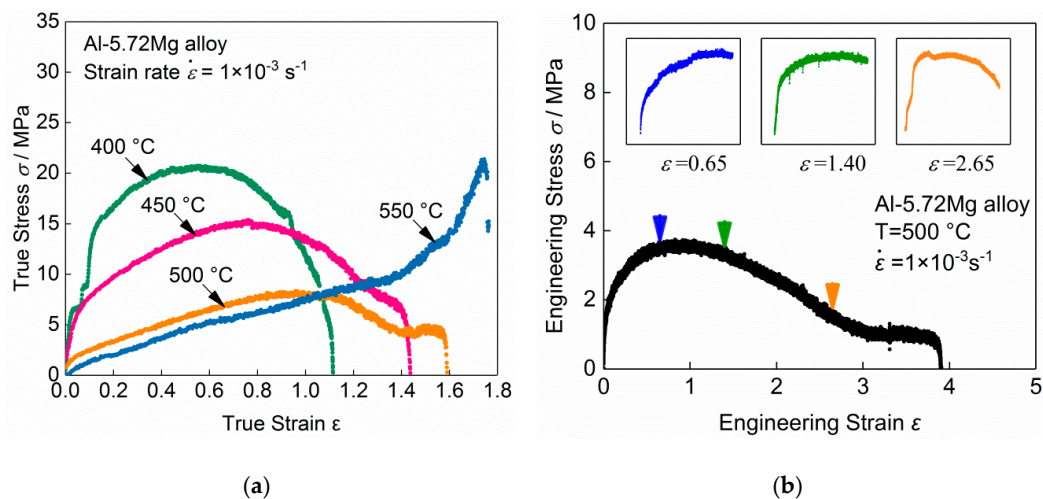


Figure 1. True stress–true strain results of 5A70 aluminum alloy at 400–550 °C and $1 \times 10^{-3} \text{ s}^{-1}$ (a), and different superplastic tensile strain stages, $\varepsilon = 0.65, 1.40$ and 2.65, at 500 °C and $1 \times 10^{-3} \text{ s}^{-1}$ (b).

Figure 1a shows that there was no obvious steady-state flow stage in the superplastic tensile state of the 5A70 alloy, as was the case for other aluminum alloys with a different magnesium content [22,23]. When the strain rate was constant, the superplastic elongation-to-failure results of the FG 5A70 alloy enlarged with the increased temperatures were $\delta = 205\%, 321\%, 390\%$ and 406%. At 550 °C, which is close to the dissolution temperature of precipitated phase particles. The reduction of the pinning effect during dynamic recrystallization because of the content of phase particles decrease. In addition, the strain hardening obviously occurred during the superplastic deformation due to the increased distortion of the grain growth, leading to an increase of true stress [24]. The strain hardening was attributed to dislocation sliding/climbing. Additionally, the dislocation density changed nonmonotonically with stable grain structure during the initial stage of the superplastic deformation. A high dislocation density at the beginning of the deformation at $T = 400 \text{ °C}$ with a high strain rate caused by grain adaptation—i.e., where the dislocation density increased rapidly and was plugged into the grain—formed dislocation walls/cells and led to increased true stress [25]. However, with the accumulation of deformations, the grain rotation occurred under shear stress and dislocations were absorbed by the grain boundaries, which led to the true stress remaining stable for a short period of time [26]. This is the reason for the true stress presenting in a step-up state. With the increasing temperature and the accumulation of superplastic deformation, the true stress increased and the strain hardening strengthened gradually and clearly.

Figure 1b demonstrates that in the initial stage of superplastic tensile, the engineering stress increases continuously and reaches its maximum at $\varepsilon = 0.65$. This is due to the large number of dislocations formed during superplastic deformation and the grain growth in high temperature and low strain rate. The maximum stress value, $\sigma_{max} = 3.75 \text{ MPa}$ as shown in Figure 1b. When the strain reached $\varepsilon = 1.40$, the applied stress gradually decreased and the superplastic deformation reached a correspondingly stable region. The applied stress slowly decreased and eventually remained low

value until the strain reached $\varepsilon = 2.65$. The data at different stages of superplastic tensile stress are provided by the test results in Figure 1b. In the last stage of the superplastic tensile, the stress value remains constant in Figure 1b and the corresponding true stress value increases continuously as shown in Figure 1a.

3.2. Cavity Nucleation

The superplastic tensile specimen was analyzed using a TEM at 500 °C and $1 \times 10^{-3} \text{ s}^{-1}$ with the strain $\varepsilon = 0.65$, as shown in Figure 2. This illustrates that the increase of stress at the initial stage of the superplastic tensile stage due to the increase of the dislocation density under the grain boundary sliding (GBS), in addition, the density of the dislocation was $\sim 3.65 \times 10^{14} \text{ m}^{-2}$.

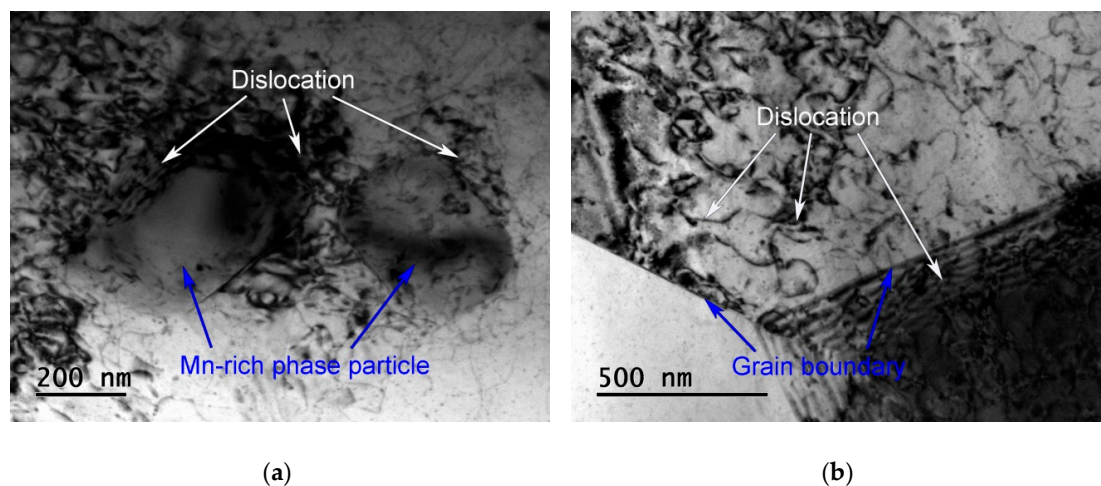


Figure 2. The relationship between the dislocations, precipitate phases (a) and grain boundaries (b) found using the TEM tests at 500 °C and $1 \times 10^{-3} \text{ s}^{-1}$ ($\varepsilon = 0.65$).

The diffusion activation energy ranged from 135 to 139 kJ/mol at temperatures ranged from 400 to 500 °C, which were close to the lattice diffusion activation energy, 143.4 kJ/mol, of pure aluminum [27]. Analysis of the superplastic behavior in terms of the diffusion activation energy and surface morphology illustrates that lattice diffusion dominates the GBS deformation mechanism of FG 5A70 alloy, and the GBS occurs through the dislocation sliding/climbing on grain boundaries. At 500 °C and $1 \times 10^{-3} \text{ s}^{-1}$, when the applied stress accumulation reached the maximum point in superplastic tensile stage, it was clearly found that under the shear stress the GBS caused dislocations to pile up near the precipitation phase, as shown in Figure 2a, and dislocations crossed the grain boundary by sliding and climbing to form a subgrain boundary, as shown in Figure 2b. The dislocation density was higher and the plugging/gathering occurred at the head of the precipitation phases, leading to the stress concentration. When the pile-up stress, σ_p , exceeded the theoretical decohesion strength of the (Al-matrix/Second phase particles) interphase boundary, a small cavity formed, and the cavity began to nucleate attached to the precipitation phase [28]. The stress at the head of the pile-up, σ_p , is given by [29]:

$$\sigma_p = \frac{2L\tau^2}{Gb}, \quad (1)$$

where L is the length of the pile-up and equivalent to the linear intercept grain size. G is the shear modulus (MPa). The pure aluminum temperature control model was adopted. In this paper, $L = d/1.74$, $\tau = \sigma/\sqrt{3}$. b is the Burgers vector, $b = a/\sqrt{2} = 2.863 \times 10^{-10} \text{ m}$ [30]. When the test temperature was 500 °C, the maximum applied stress ($\sigma_{max} = 3.75 \text{ MPa}$) solution was plugged into the type product stress $\sigma_p = 7.87 \text{ MPa}$. The plugging stress threshold was more than twice the applied stress in the superplastic tensile state. It is obvious that the Al matrix and the strengthening phase particles were easily separated, which promoted the cavity nucleation under the different stress levels. In addition,

dislocations coalesced at the grain boundary to form a subgrain boundary, as showed in Figure 2b. It is assumed that the shape of the cavity is circular and the equivalent radius of the cavity is r . The change of the Helmholtz free energy of the system was obtained as follows [27,31,32]:

$$\Delta G = -2.53\left(\frac{2}{3} \times \frac{d}{1.74b} \times \frac{\sigma^2}{G}\right)r^3 + (9.31\gamma - 0.5 \times 2.93\gamma) - 3.79 \times \frac{\left(\frac{2}{3} \times \frac{d}{1.74b} \times \frac{\sigma^2}{G}\right)^2}{2E}r^3, \quad (2)$$

where γ is the surface energy of the cavity, d is the grain size and E is the Young's modulus of pure aluminum. Figure 3 shows the change of the Helmholtz free energy as a function of the cavity radius of the 5A70 alloy deformed at different tensile temperatures, with the strain $\varepsilon = 0.3$ and the strain rate was $\dot{\varepsilon} = 1 \times 10^{-3} \text{ s}^{-1}$. By increasing the tensile temperature range from 400 to 550 °C, the maximum values of the Helmholtz free energy ranged from 8.32×10^{-16} to 8.41×10^{-14} J, and the corresponding critical radius of the cavity nucleation maximum values increased from 2.16×10^{-8} to 2.37×10^{-7} m, indicating that the cavity was very different and nucleated at a higher superplastic tensile temperature. That is, at 500–550 °C, it was more difficult for the cavity to cross the nucleation barrier than at 400–450 °C. According to Figure 1a, it is suggested that when the superplastic tensile temperatures were 500 and 550 °C, the strain hardening led to an increase of the true stress. Meanwhile, the cavity nucleation was beneficial to the superplastic flow.

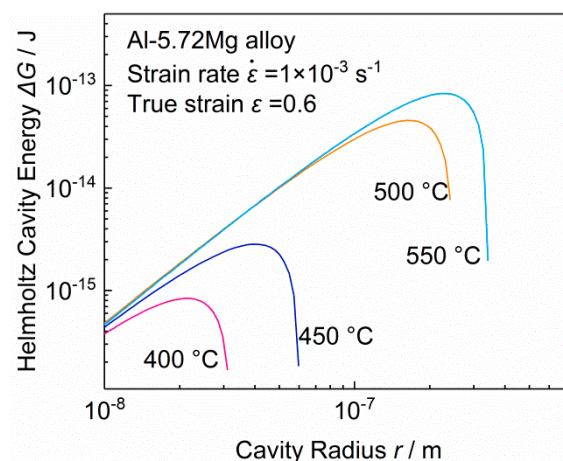


Figure 3. The relationship between the nucleation free energy and cavity radius of 5A70 aluminum alloy in the superplastic tensile state (400–550 °C).

3.3. Cavity Growth

3.3.1. Cavity Growth Controlled by Diffusion and Plastic

The mechanism of cavity growth in the superplastic tensile state is divided into two types: (1) the growth mechanism of stress promoting a spherical cavity growing by diffusion along the grain boundary; and (2) the cavity growth is controlled by the plastic flow of the surrounding material [27,32–35].

At 500 °C and $1 \times 10^{-3} \text{ s}^{-1}$, the parallel sections of the superplastic tensile specimens were tested by the SEM with an aborted strain of $\varepsilon = 0.65$, 1.40 and 2.65; the corresponding results are presented in Figure 4. There are a large number of finely-dispersed second phase particles in the 2 mm thick deformed sheet, and the black points/areas show the cavity distribution during the superplastic tensile deformation. It is clear that the number and density of the cavities increased immediately, accompanied by the constant accumulation of the deformation in Figure 4a,c,e. In addition, the corresponding magnification is shown in Figure 4b,d,f.

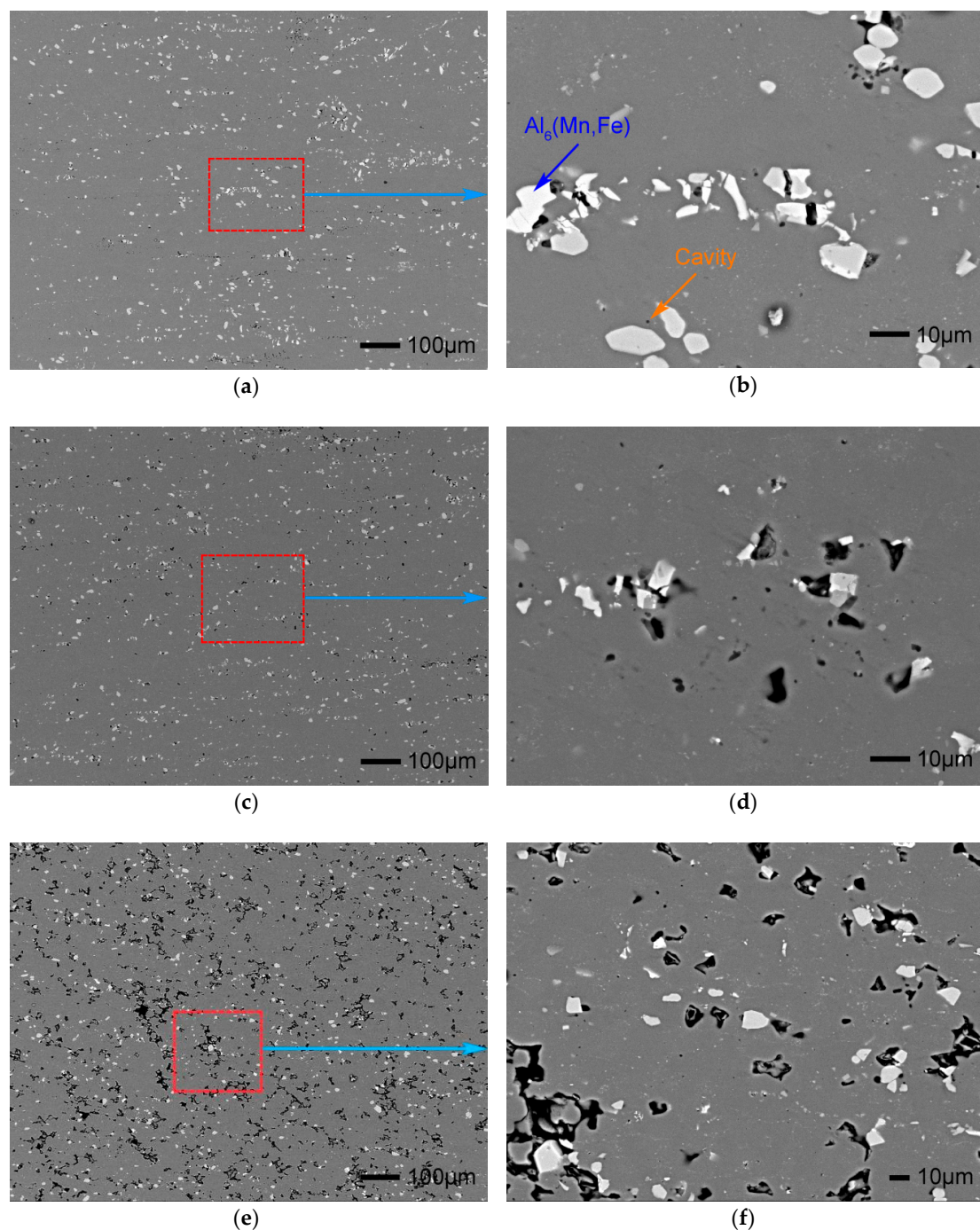


Figure 4. The scanning electron microscopy results in the superplastic tensile stages and magnified regions at 500 °C and $1 \times 10^{-3} \text{ s}^{-1}$: $\epsilon = 0.65$ (a,b), $\epsilon = 1.40$ (c,d) and $\epsilon = 2.65$ (e,f).

Figure 4b,d shows the cavity growth with a strain increase from $\epsilon = 0.65$ to 1.40, and the cavities evidently grew and interlinked at $\epsilon = 2.65$ in Figure 4e,f. The initial nucleation stage of the cavity mostly exhibited an O-shape due to the low surface energy of the spherical cavity, which remained relatively stable and easy to nucleate. O-shaped cavities were found at every stage, indicating that new cavity nucleation continued to occur during the process of strain accumulation in the superplastic tensile stage, as shown in Figure 4b,d,f.

At 500 °C and $1 \times 10^{-3} \text{ s}^{-1}$, it is suggested that the applied stress reached the maximum value at $\epsilon = 0.65$, as shown in Figure 1b. This is because the dislocations continuously accumulated in the second phase particles and the grain boundaries during deformation, as shown in Figure 2, which increased the

strength of the 5A70 alloy and provided the driving force for cavity nucleation. Meanwhile, Mg atoms precipitated from the Al-matrix to form second phase particles. The pinning effect of the precipitated phase was encouraged to enhance the cavity nucleation and the chemical potential between the forceful grain boundary atoms and the free surface of the cavity [34,35]. However, the cavity growth rate under diffusion control was obtained as follows:

$$\frac{dr}{d\varepsilon} = \alpha_0 \left(\frac{2\Omega\delta D_{gb}}{r^2 kT} \right) \left[\frac{\sigma - (2\gamma/r)}{\dot{\varepsilon}} \right], \quad (3)$$

where Ω is the atomic volume, δ is the grain boundary width, $\delta = 2b$. D_{gb} is the coefficient for grain boundary diffusion, k is Boltzmann's constant, T is the absolute temperature, σ is the applied stress, γ is the surface energy, r is the cavity radius, α_0 is the cavity spacing, $\dot{\varepsilon}$ is the strain rate and α_0 is defined as $\alpha_0 = 1 / \{4 \ln(a/2r) - [1 - (2r/a)^2][3 - (2r/a)^2]\}$. The cavity size parameter was $\alpha_0 = 0.12$ as the initial stage of cavity diffusion complied with $a/2r \geq 10$.

The cavities grew due to plastic deformation in the surrounding crystalline lattice. The plastic-controlled growth mechanism is given by [33–35]:

$$\frac{dr}{d\varepsilon} = r - \frac{3\gamma}{2\sigma}, \quad (4)$$

where the superplastic tensile of 5A70 aluminum alloy was tested at 400–500 °C, and the critical cavity radius, r_c , denoting the transition from conventional diffusion growth for plastic-controlled growth was obtained from Formulas (3) and (4), so that [27,33]:

$$r_c = \left(\frac{2\Omega\delta D_{gb}}{kT} \right)^{\frac{1}{3}} \left(\frac{\sigma}{\dot{\varepsilon}} \right)^{\frac{1}{3}}, \quad (5)$$

Formula (5) demonstrates that when the temperature and strain rate are constant, the lower the applied stress in the superplastic tensile deformation, and the smaller the critical cavity radius, r_c , exhibited. Figure 4 shows the tension strain $\varepsilon = 0.65, 1.40$ and 2.65 , presenting the results of the SEM analysis as pointed in the Figure 1b. As noted above, the accumulation of tensile deformation causes a decrease in the critical nucleation radius, moreover, the cavity density increases immediately. This is a complex function of cavity nucleation related to the testing temperature, strain rate, microstructure size and phase-particle shape and size. Generally, larger particles and larger interfacial defects cause a more rapid separation of the Al-matrix and second phase particles with an increase in tensile deformation, while smaller particles have a smaller restricted plastic zone, and greater accumulated strain is needed to produce complete separation for continuous cavity nucleation [36,37]. Taking the data in Table 2 into Formulas (3) and (4), the cavity growth rate, $dr/d\varepsilon$, can be drawn as shown in Figure 5.

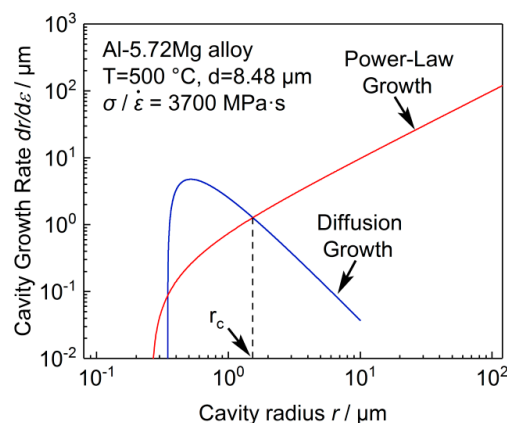


Figure 5. Schematic illustration of diffusion growth and plastic-controlled growth, showing the critical radius r_c .

Table 2. Constants used for the calculation of the cavity growth rate ($dr/d\varepsilon$).

Temperature $T/^\circ\text{C}$	Applied Stress σ/MPa	Strain-Rate Sensitivity m	Atomic Volume V/m^3	Strain Rate $\dot{\varepsilon}/\text{s}^{-1}$
500	3.70	0.47	2.34×10^{-2}	1×10^{-3}

* The material constants used for 5A70 alloy: $\delta = 5.72 \times 10^{-10}$ m, $k = 1.38 \times 10^{-23}$ J·K⁻¹, $D_{gb} = 3.3 \times 10^{-14}$ m²·s⁻¹, $\gamma = 0.64$ J·m⁻² and $R = 8.314$ J·mol⁻¹·K⁻¹.

Figure 5 shows the relationship between the cavity growth rate, $dr/d\varepsilon$, and the cavity radius, r , indicating the mechanism of cavity growth during the superplastic tensile state of FG 5A70 alloy. The figure illustrates that when the cavity radius $r < r_c = 1.52$ μm , the cavity growth controlled by diffusion dominates the cavity growth mechanism. By contrast, the cavity growth is controlled by the plastic flow, exhibiting a power-law growth rate that is larger than the other type of growth rate. In addition, during plastic-controlled cavity growth the cavity volume fraction should increase exponentially with strain, and η is the growth rate parameter for the cavity volume [38,39].

$$\eta = \frac{3m+1}{2} \frac{\sinh \frac{2(2-m)}{3(2+m)}}{m} \quad (6)$$

The coefficient of strain rate sensitivity, m , value continuously decreases along with the accumulation of tensile deformation. However, the cavity growth rate parameter increases as the strain increases simultaneously. Figure 6 shows the true strain range from $\varepsilon = 0.1$ to 1.6, while the growth rate parameters increased correspondingly, from $\eta = 1.21$ to 3.22. Therefore, the diffusion-controlled cavity growth with a small growth rate parameter occurred in the initial stage of superplastic tensile deformation. As the plastic-controlled growth dominated the cavity growth, the cavity growth rate parameter and the cavity growth rate increased simultaneously. Meanwhile, it was clearly found that plastic-controlled growth of the cavities occurred mainly due to cavity interlinkage and coalescence.

3.3.2. Effect of Superplastic Diffusion on Cavity Growth

Along with superplastic tensile deformation, the Mg atoms continuously separated from the distorted Al-matrix lattice into the generated vacancies. When the cavity size of the diffusion mechanism was larger than the grain size, the newly formed vacancies diffused into the neighboring cavity along the multiple grain boundaries under stress. Meanwhile, superplastic diffusion growth of the cavity nucleation region appeared, and then the cavities begin to interlink during the growth process. Superplastic diffusion growth was the dominant mechanism during this stage, when the voids vacated into the adjacent cavities, subject to diffusion-controlled growth.

Chokshi et al. [35] noted that the growth of cavities due to superplastic diffusion occurred while the cavity was large enough to intersect with multiple grain boundaries. This required a cavity size larger than half of the grain size, $d/2$, therefore, the grain size of cavity growth under superplastic diffusion was considered between $d/2$ and d .

Figure 6 shows comprehensively the cavity growth parameter, η , cavity area fraction, S_c , and the grain diameter radius, d , with the cavity equivalent radius, r . Meanwhile, the corresponding S_c was presumed to be 0.24, 0.77 and 3.96%, as shown in Figure 4a,c,e.

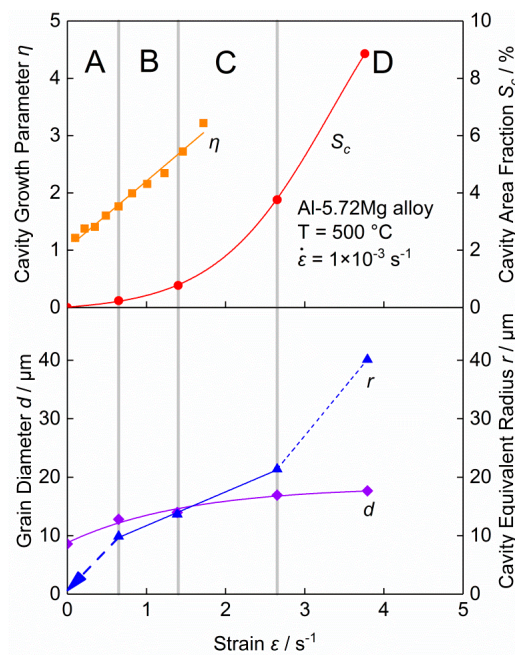


Figure 6. The cavity growth parameter, η , cavity area fraction, S_c , cavity equivalent radius, r , and dynamic recrystallization grain size, d , at different superplastic tensile stages at 500 °C and $1 \times 10^{-3} s^{-1}$.

Region A in Figure 6 shows an increase in the applied stress due to increased dislocation and the continuous nucleating of the cavity (Figure 4) at the tensile strain stage $\epsilon = 0-0.65$, corresponding to cavity equivalent radius $r = 9.76 \mu m$ and grain size $d = 12.83 \mu m$. The dominant mechanism of cavity growth transformed from diffusion growth to superplastic diffusion growth, judging by the inequality $r_c \leq d/2 \leq r \leq d$. In region B, with a tensile strain of $\epsilon = 0.65-1.40$, the applied stress continued to decline due to the cavity nucleation and cavity growth. Superplastic diffusion growth took effect because the cavity radius complied with $d/2 \leq r \approx d$, while the cavity equivalent radius was $r = 13.90 \mu m$ and the grain size was $d = 13.96 \mu m$ at tensile strain $\epsilon = 1.40$. Figure 6 shows the cavity growth parameter, η , corresponding to the coefficients of strain rate sensitivity, m , which are distributed in the region A and region B. Therefore, superplastic diffusion growth dominated the cavity growth of tensile strain $\epsilon = 0.46-1.40$. Ultimately, the plastic-controlled growth dominated the cavity growth, interlinkage and coalescence, when the superplastic tensile strain was $\epsilon > 1.40$, as shown in region C and D.

Figure 6 demonstrates that dynamic recrystallization occurred during superplastic tensile deformation. Due to the pinning effect of a large number of dispersed Mg-rich phase particles, the grain size was $8.6 \mu m$ after rolling and $17.67 \mu m$ after superplastic fracture in the ND plane. The cavity size increased continuously related to the superplastic diffusion growth. Previous analysis in Figure 4b,d indicated that the cavity nucleation and growth was not interlinked extensively. However, the cavities interlinked and coalesced rapidly due to the cavity equivalent radius, r , being larger than the grain size, d , which coincided with the previous analysis in Figure 4f.

3.3.3. Effect of the Fine-Grained Structure on Cavity Growth

The above analyses showed that the fine-grained structure played an important part in the superplastic diffusion growth and plastic-controlled growth. Figure 7a showed that fully dynamic recrystallization occurred during the superplastic tensile deformation and the grain size increased, while the result for $\epsilon = 2.65$ illustrated that the grain size fraction of $d = 20-30 \mu m$ was clearly much higher than $\epsilon = 0.65$ and 1.40 . It is well-known that the glide plane of the face-centered cubic crystal of FG 5A70 alloy is $\{111\}$, and the grain boundary slip direction is $\langle 110 \rangle$ [40]. Meanwhile, in order to satisfy the balance of grain-to-grain deformation and the balance of the reaction stress in the superplastic

tensile state, the GBS occurred mainly in the sliding direction. This clearly clarified the grain rotation and the GBS in the superplastic tensile state of the FG 5A70 alloy, as illustrated in Figure 7b [41].

Figure 7b shows that the fraction of the grain boundary angle at 3.58° was 20.3% ($\varepsilon = 2.65$), which was greater than 5.41% ($\varepsilon = 0.65$) and 3.83% ($\varepsilon = 1.40$). Plastic-controlled growth dominated the cavity interlinkage during deformation because the fraction of large cavities increased obviously from $\varepsilon = 0.65$ to 2.65, as shown in Figure 7c. At $\varepsilon = 2.65$, the cavity area fraction of 20–200 μm^2 was significantly higher than $\varepsilon = 0.65$ and 1.40. This demonstrated that the cavity coalescence formed a larger cavity, which was detrimental to the superplastic tensile state and eventually led to cracking.

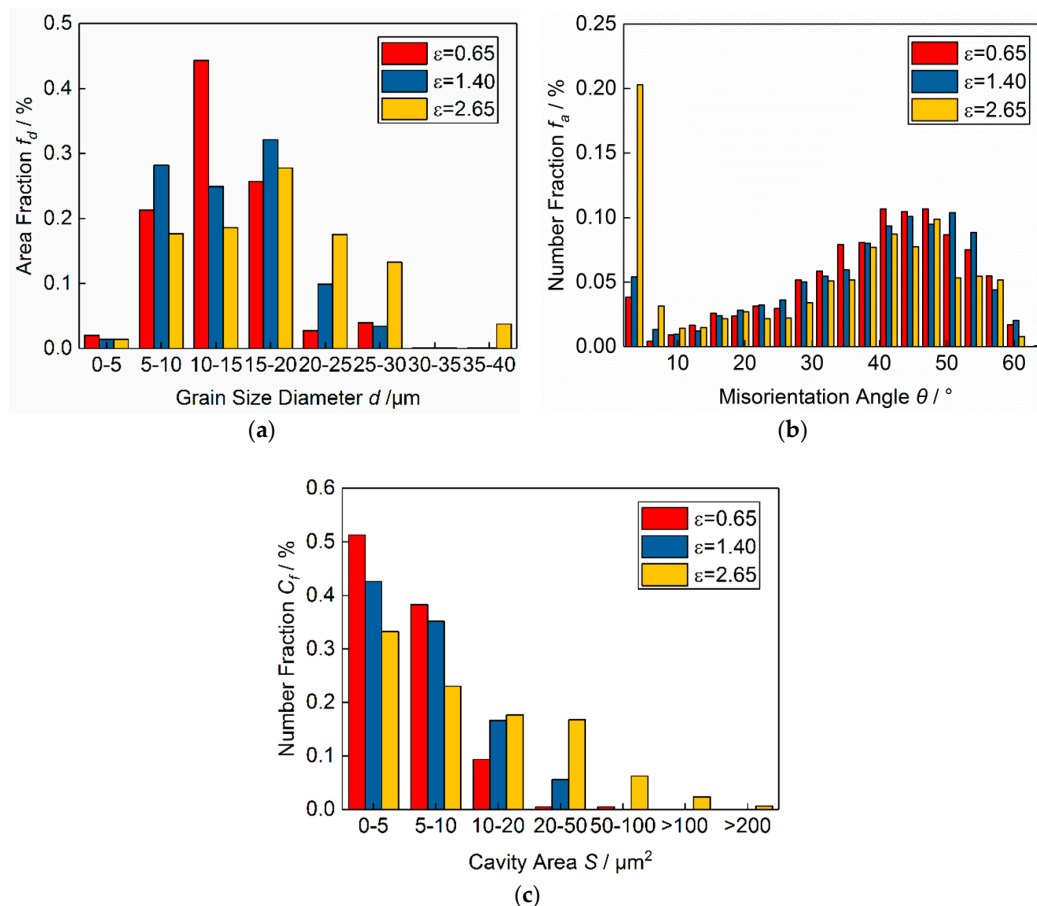


Figure 7. Distribution of the strain due to grain boundary sliding in (a) the dynamic recrystallization grain size, (b) the grain boundary angle rotation and (c) the number of cavity fraction in different strain stages. The superplastic tensile condition was 500 °C and $1 \times 10^{-3} \text{ s}^{-1}$ of fine-grained 5A70 alloy.

3.4. Crack Formation

In the present investigation, detailed data were obtained on the formation and development of cavity behavior, suggesting that plastic-controlled growth dominated the cavity interlinkage and coalescence. This was expected to result in crack formation and to influence the superplastic elongation-to-failure of the studied 5A70 alloy.

Figure 8a–h illustrates the testing results of the EBSD close to the fracture locations with different temperatures ranging from 400 to 550 °C, and the strain rate was $1 \times 10^{-3} \text{ s}^{-1}$. Correspondingly, Figure 8i–l shows the morphology tested by the SEM at 5 mm from the superplastic fracture location.

Figure 8 shows the EBSD analyses of the 5A70 alloy deformed at different temperatures at $\dot{\varepsilon} = 1 \times 10^{-3} \text{ s}^{-1}$ after superplastic fracture. The color of each grain was coded by its crystal orientation based on the [001] inverse pole figure, as seen in Figure 8a. There was an aggregation of a large number of ultrafine grains near the small cavities, in addition, the cavity interlinkage and coalescence were

precisely identified via supporting microscopy evidence. Nevertheless, new ultrafine grains occurred in limited regions and generated near initial deformed grains, indicating that dynamic recrystallization had occurred. Figure 8a,c,f,g shows that the microstructure consisted mainly of a grain size larger than $10\ \mu\text{m}$. It can be clearly seen in Figure 8a,c,e,g that the grain size of the FG 5A70 alloy increased with the increased temperature and the superplastic tensile deformation, while the grain sizes were 9.60 , 11.78 , 13.32 and $21.16\ \mu\text{m}$. At $400\ ^\circ\text{C}$ and $1 \times 10^{-3}\ \text{s}^{-1}$, dynamic recrystallization occurred without obvious grain growth. However, in this work the final grain structure had an average recrystallized grain size of less than $15\ \mu\text{m}$ at $400\text{--}500\ ^\circ\text{C}$, revealing that the 5A70 alloy had a strong ability to inhibit grain growth during superplastic deformation. At $550\ ^\circ\text{C}$, the content of Mg-rich phase particles decreased and the abnormal grain growth could be inhibited due to the reduction of the pinning effect during dynamic recrystallization. Therefore, the plastic deformation of the grain growth in the superplastic tensile direction dominated the grain growth and led to crack formation caused by cavity coalescence, as shown in Figure 8g.

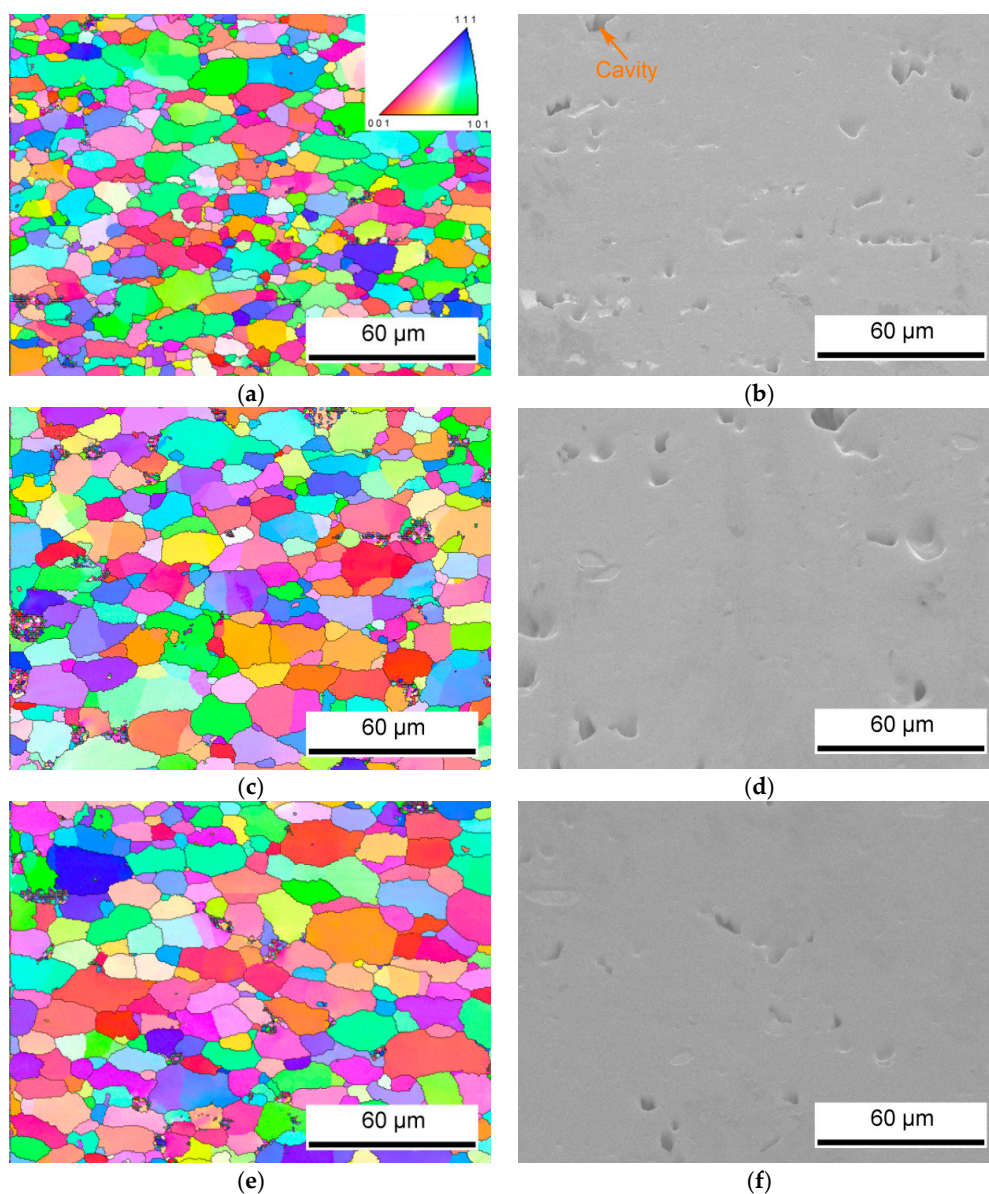


Figure 8. Cont.

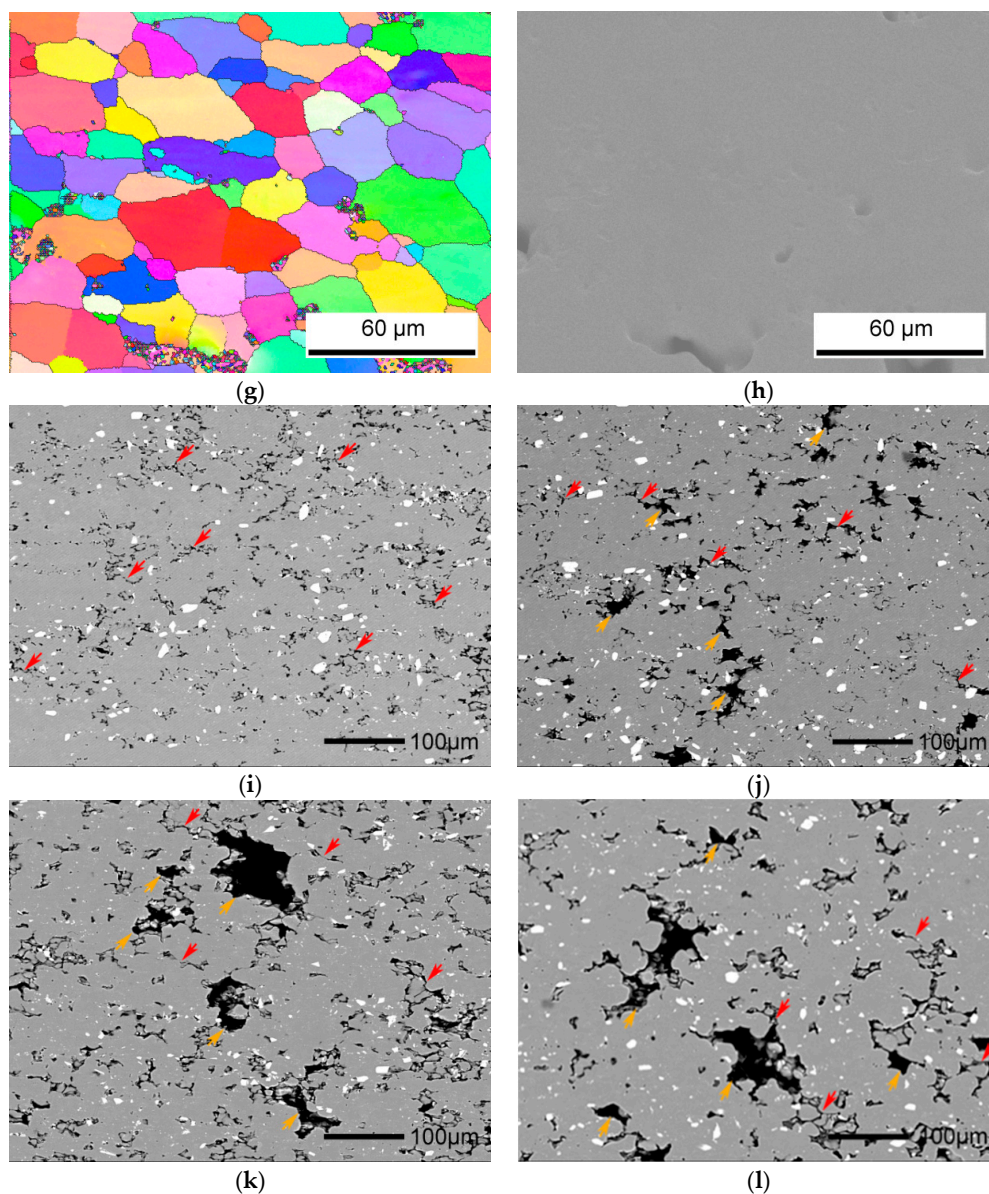


Figure 8. The Grain structures and the superplastic fracture morphologies at initial strain rate $1 \times 10^{-3} \text{ s}^{-1}$ with different temperatures: 400 °C (a,b,i), 450 °C (c,d,j), 500 °C (e,f,k) and 550 °C (g,h,l).

In Figure 8i–l it can be seen that the cavities nucleated tightly attached to the particles, the cavity growth interlinked in the superplastic tensile state, indicated by red arrows, and the cavities coalesced, indicated by the yellow arrows. Comparing Figure 4a,c,e and Figure 8a,c,e, it is suggested that with the continuous precipitation of Mg-rich phase particles at the grain boundaries, the new cavities nucleated continuously in the superplastic tensile state. Meanwhile, the cavity area fractions in Figure 8i–k of 1.79, 4.07 and 8.66% increased with temperatures of 400, 450 and 500 °C, respectively. There was a large amount of cavity nucleation and growth along with the accumulation of tensile deformations, as shown in Figure 8i–l. Due to the decrease of second phase particles, it was clearly found that the increase in the grain sizes had a certain effect in terms of promoting the absorption of small cavities at 550 °C and $1 \times 10^{-3} \text{ s}^{-1}$, while the cavity area fraction was 5.66% as shown in Figure 8l. Based on this research, it can be stated that cavity nucleation, growth, interlinkage and coalescence, along with the accumulation of tensile deformation, cause crack formation, resulting in the superplastic fracture of FG 5A70 alloys.

4. Conclusions

The following conclusions can be drawn from this work:

- (1) Strain hardening occurs in fine-grained 5A70 alloys in the superplastic tensile state at temperatures ranging from 400 to 550 °C, when the strain rate is $1 \times 10^{-3} \text{ s}^{-1}$.
- (2) The dislocation density of the fine-grained 5A70 alloy was $\sim 10^{14} \text{ m}^{-2}$, which piled up at the head of the second phase particles and the grain boundaries, resulting in the increase of true stress and the nucleation of the cavities.
- (3) Cavity growth mainly occurred at the stage of diffusion growth and superplastic diffusion growth due to the diffusion of the voids into adjacent cavities with a cavity radius smaller than the grain size.
- (4) Plastic-controlled growth dominated the cavity interlinkage and coalescence process, which eventually led to superplastic fractures.
- (5) At 500 and 550 °C, the abnormal grain growth of FG 5A70 alloy during dynamic recrystallization was higher than 400 and 450 °C due to the decrease in Mg-rich phase particles and the Helmholtz free energies.

Author Contributions: Conceptualization, Z.H. and S.L.; methodology, S.L.; software, S.L.; validation, Z.H., S.J. and S.L.; formal analysis, S.L.; investigation, S.L.; resources, Z.H. and S.J.; data curation, S.L.; writing—original draft preparation, S.L.; writing—review and editing, S.L.; supervision, H.Z.; project administration, S.J.; funding acquisition, S.J.

Funding: This research is funded by the Fundamental Research Funds for the Central Universities of China, Grant number FRF-TP-16-043A1 and the APC was funded by S.J.

Acknowledgments: We would like to thank Guoliang Xie for his help in the material preparation, Xuotong Zhao for his assistance with the superplastic tensile tests, Shuming Wang for his assistance with the SEM/EBSD analysis, and Xinqin Liu for her help with the analysis of the results.

Conflicts of Interest: The authors declare no conflict of interest.

References

1. Bolt, P.J.; Lamboo, N.A.P.M.; Rozier, P.J.C.M. Feasibility of warm drawing of aluminium products. *J. Mater. Process. Technol.* **2001**, *115*, 118–121. [[CrossRef](#)]
2. Naka, T.; Torikai, G.; Hino, R.; Yoshida, F. The effects of temperature and forming speed on the forming limit diagram for type 5083 aluminum–magnesium alloy sheet. *J. Mater. Process. Technol.* **2001**, *113*, 648–653. [[CrossRef](#)]
3. Tokuda, M.; Inaba, T.; Ohigashi, H.; Kurakake, A. Discussions on constitutive equations of superplastic 5083 aluminum alloy. *Int. J. Mech. Sci.* **2001**, *43*, 2035–2046. [[CrossRef](#)]
4. Beijing Institute of Aeronautical Materials Group. *Materials Technology of Aeronautics*; Aviation Industry Press: Beijing, China, 2014; pp. 131–143. ISBN 978-7-5165-0298-3.
5. Smolej, A.; Klobčar, D.; Skaza, B.; Nagode, A.; Slaček, E.; Dragojević, V.; Smolej, S. Superplasticity of the rolled and friction stir processed Al–4.5 Mg–0.35Sc–0.15Zr alloy. *Mater. Sci. Eng. A* **2014**, *590*, 239–245. [[CrossRef](#)]
6. Charit, I.; Mishra, R.S. Evaluation of microstructure and superplasticity in friction stir processed 5083 Al alloy. *J. Mater. Res.* **2004**, *19*, 3329–3342. [[CrossRef](#)]
7. Lee, Y.B.; Shin, D.H.; Park, K.T.; Nam, W.J. Effect of annealing temperature on microstructures and mechanical properties of a 5083 Al alloy deformed at cryogenic temperature. *Scr. Mater.* **2004**, *51*, 355–359. [[CrossRef](#)]
8. Verma, R.; Ghosh, A.K.; Kim, S.; Kim, C. Grain refinement and superplasticity in 5083 Al. *Mater. Sci. Eng. A* **1995**, *191*, 143–150. [[CrossRef](#)]
9. Soer, W.A.; Chezan, A.R.; Hosson, J.T.M.D. Deformation and reconstruction mechanisms in coarse-grained superplastic Al–Mg alloys. *Acta Mater.* **2006**, *54*, 3827–3833. [[CrossRef](#)]
10. Hasegawa, T.; Yasuno, T.; Nagai, T.; Takahashi, T. Origin of superplastic elongation in aluminum alloys produced by mechanical milling. *Acta Mater.* **1986**, *46*, 6001–6007. [[CrossRef](#)]

11. Orozco-Caballero, A.; Ruano, O.A.; Rauch, E.F.; Carreño, F. Severe friction stir processing of an Al-Zn-Mg-Cu alloy: Misorientation and its influence on superplasticity. *Mater. Des.* **2018**, *137*, 128–139. [[CrossRef](#)]
12. Patel, V.V.; Badheka, V.; Kumar, A. Effect of polygonal pin profiles on friction stir processed superplasticity of AA7075 alloy. *J. Mater. Process. Technol.* **2017**, *240*, 68–76. [[CrossRef](#)]
13. Wang, Y.; Mishra, R.S. Finite element simulation of selective superplastic forming of friction stir processed 7075 Al alloy. *Mater. Sci. Eng. A* **2007**, *463*, 245–248. [[CrossRef](#)]
14. Garcia-Infanta, J.M.; Zhilyaev, A.P.; Sharafutdinov, A.; Ruano, O.A.; Carreño, F. An evidence of high strain rate superplasticity at intermediate homologous temperatures in an Al-Zn-Mg-Cu alloy processed by high-pressure torsion. *J. Alloy. Compd.* **2009**, *473*, 163–166. [[CrossRef](#)]
15. Li, S.; Huang, Z.G.; Jin, S.Y.; Wang, B.Y.; Liu, X.Q.; Lei, K. Heat Treatment Process of Cold Rolled 5A70 Aluminum alloy Superplastic Sheet. *Chin. J. Rare. Met.* **2018**, *42*, 283–288. [[CrossRef](#)]
16. Chokshi, A.H.; Langdon, T.G. The influence of rolling direction on the mechanical behavior and formation of cavity stringers in the superplastic Zn-22% Al alloy. *Acta Metall.* **1989**, *37*, 715–723. [[CrossRef](#)]
17. Nieh, T.G.; Hsiung, L.M.; Wadsworth, J.; Kaibyshev, R. High strain rate superplasticity in a continuously recrystallized Al-6%Mg-0.3%Sc alloy. *Acta Mater.* **1998**, *46*, 2789–2800. [[CrossRef](#)]
18. Pilling, J.; Ridley, N. Effect of hydrostatic pressure on cavitation in superplastic aluminium alloys. *Acta Metall.* **1986**, *34*, 669–679. [[CrossRef](#)]
19. Chen, C.L.; Tan, M.J. Cavity growth and filament formation of superplastically deformed Al 7475 Alloy. *Mater. Sci. Eng. A* **2001**, *298*, 235–244. [[CrossRef](#)]
20. Conrad, H.; Cao, W.D.; Lu, X.P.; Sprecher, A.F. Effect of electric field on cavitation in superplastic aluminum alloy 7475. *Mater. Sci. Eng. A* **2001**, *138*, 247–258. [[CrossRef](#)]
21. Engler, O.; Kuhnke, K.; Hasenclever, J. Development of intermetallic particles during solidification and homogenization of two AA 5xxx series Al-Mg alloys with different Mg contents. *J. Alloy. Compd.* **2017**, *728*, 669–681. [[CrossRef](#)]
22. Duan, Y.L.; Xu, G.F.; Xiao, D.; Zhou, L.Q.; Deng, Y.; Yin, Z.M. Excellent superplasticity and deformation mechanism of Al-Mg-Sc-Zr alloy processed via simple free forging. *Mater. Sci. Eng. A* **2015**, *624*, 124–131. [[CrossRef](#)]
23. Lee, S.; Utsunomiya, A.; Akamatsu, H.; Neishi, K.; Furukawa, M.; Horita, Z.; Langdon, T.G. Influence of scandium and zirconium on grain stability and superplastic ductilities in ultrafine-grained Al-Mg alloys. *Acta Mater.* **2002**, *50*, 553–564. [[CrossRef](#)]
24. Horita, Z.; Furukawa, M.; Nemoto, M.; Barnes, A.J.; Langdon, T.G. Superplastic forming at high strain rates after severe plastic deformation. *Acta Mater.* **2000**, *48*, 3633–3640. [[CrossRef](#)]
25. Gashti, S.O.; Fattah-alhosseini, A.; Mazaheri, Y.; Keshavarz, M.K. Effects of grain size and dislocation density on strain hardening behavior of ultrafine grained AA1050 processed by accumulative roll bonding. *J. Alloy. Compd.* **2016**, *685*, 854–861. [[CrossRef](#)]
26. Mikhaylovskaya, A.V.; Yakovtseva, O.A.; Golovin, I.S.; Pozdniakov, A.V.; Portnoy, V.K. Superplastic deformation mechanisms in fine-grained Al-Mg based alloys. *Mater. Sci. Eng. A* **2015**, *627*, 31–41. [[CrossRef](#)]
27. Cao, F.R.; Li, Z.L.; Zhang, N.X.; Ding, H.; Yu, F.X.; Zuo, L. Superplasticity, flow and fracture mechanism in an Al-12.7Si-0.7Mg alloy. *Mater. Sci. Eng. A* **2013**, *571*, 167–183. [[CrossRef](#)]
28. Chokshi, A.H. Cavity nucleation and growth in superplasticity. *Mater. Sci. Eng. A* **2005**, *410–411*, 95–99. [[CrossRef](#)]
29. Cao, F.R. *Metal Superplasticity*; Metallurgical Industry Press: Beijing, China, 2014; pp. 211–212, ISBN 978-7-5024-6690-9.
30. Langdon, T.G. A unified approach to grain boundary sliding in creep and superplasticity. *Acta Mater.* **1994**, *42*, 2437–2443. [[CrossRef](#)]
31. Mohamed, F.A. Interpretation of superplastic flow in terms of a threshold stress. *J. Mater. Sci.* **1983**, *18*, 582–592. [[CrossRef](#)]
32. Raj, R.; Ashby, M.F. Intergranular fracture at elevated temperature Rupture intergranulaire aux températures elevees Intergranularer Bruch bei Höheren Temperaturen. *Acta Metall.* **1975**, *23*, 653–666. [[CrossRef](#)]
33. Bae, D.H.; Ghosh, A.K. Cavity formation and early growth in a superplastic Al-Mg alloy. *Acta Mater.* **2002**, *50*, 511–523. [[CrossRef](#)]
34. Kawasaki, M.; Xu, C.; Langdon, T.G. An investigation of cavity growth in a superplastic aluminum alloy processed by ECAP. *Acta Mater.* **2005**, *53*, 5353–5364. [[CrossRef](#)]

35. Chokshi, A.H.; Langdon, T.G. A model for diffusional cavity growth in superplasticity. *Acta Metall.* **1987**, *35*, 1089–1101. [[CrossRef](#)]
36. Liu, Z.Y. A new model for cavity nucleation. *Trans. Nonferrous Met. Soc. China.* **1997**, *7*, 145–148.
37. Ghosh, A.K.; Bae, D.H.; Materials, S.L. Initiation and Early Stages of Cavity Growth during Superplastic and Hot Deformation. *Mater. Science Forum.* **1999**, *304–306*, 609–616. [[CrossRef](#)]
38. Lee, C.J.; Huang, J.C. Cavitation characteristics in AZ31 Mg alloys during LTSP or HSRSP. *Acta Mater.* **2004**, *52*, 3111–3122. [[CrossRef](#)]
39. Takigawa, Y.; Aguirre, J.V.; Taleff, E.M.; Higashi, K. Cavitation during grain-boundary-sliding deformation in an AZ61 magnesium alloy. *Mater. Sci. Eng. A* **2008**, *497*, 139–146. [[CrossRef](#)]
40. Mao, W.; Yu, Y. Effect of elastic reaction stress on plastic behaviors of grains in polycrystalline aggregate during tensile deformation. *Mater. Sci. Eng. A* **2004**, *367*, 277–281. [[CrossRef](#)]
41. Masuda, H.; Kanazawa, T.; Tobe, H.; Sato, E. Dynamic anisotropic grain growth during superplasticity in Al–Mg–Mn alloy. *Scr. Mater.* **2018**, *149*, 84–87. [[CrossRef](#)]



© 2018 by the authors. Licensee MDPI, Basel, Switzerland. This article is an open access article distributed under the terms and conditions of the Creative Commons Attribution (CC BY) license (<http://creativecommons.org/licenses/by/4.0/>).